Proteoform-Resolved Phosphorylation Dynamics in Kinase Complexes by Hybrid Precision Mass Spectrometry

Boris Krichel*[1,2,3,4,6], Hsin-Ju Chan[5], Liam Bandura[5], Zhan Gao[5], Man-Di Wang[5], Holden T. Rogers[5], Sean J. Mcilwain[7,8], Charlotte Uetrecht[4,6] and Ying Ge*[1,2,5]

[1] Department of Cell and Regenerative Biology, School of Medicine and Public Health, University of Wisconsin-Madison, Madison, Wisconsin, USA. [2]Human Proteomics Program, School of Medicine and Public Health, University of Wisconsin-Madison, Madison, Wisconsin, USA. [3] Faculty V: School of Life Sciences, University of Siegen, 57076 Siegen, Germany. [4]CSSB Centre for Structural Systems Biology, Deutsches Elektronen Synchroton DESY, Leibniz Institute of Virology and University of Lübeck, Notkestraße 85, 22607 Hamburg, Germany. [5]Department of Chemistry, University of Wisconsin-Madison, Madison, Wisconsin, USA. [6]Institute of Chemistry and Metabolomics. University of Lübeck, 23562 Lübeck, Germany. [7]Department of Biostatistics and Medical Informatics, University of Wisconsin-Madison, Madison, WI 53705, United States. [8]University of Wisconsin Carbone Cancer Center, University of Wisconsin-Madison, Madison, WI 53705, United States.

*Corresponding authors: Dr. Boris Krichel: boris.krichel@cssb-hamburg.de ; Dr. Ying Ge: ying.ge@wisc.edu

ABSTRACT

Protein phosphorylation creates functionally distinct proteoforms through complex modification cascades, yet capturing their temporal dynamics and combinatorial patterns remains a major analytical challenge. Here, we introduce a hybrid precision mass spectrometry (MS) strategy that integrates intact mass measurements for temporal tracking, bottom-up MS analysis for site-specific kinetics, and top-down MS sequencing for proteoform characterization to resolve phosphorylation dynamics within intact kinase complexes. Using AMP-activated protein kinase (AMPK) as a model system, we uncover coordinated autophosphorylation cascades exhibiting kinetic hierarchies, with α1-S496 showing the highest kinetic efficiency. Allosteric ADaM-site activation bypasses canonical α1-T183 phosphorylation, enabling autophosphorylation even in activation-deficient mutants. Top-down MS sequencing identifies the predominant β1 proteoform as S24/25+S108 double phosphorylation, a pattern linking extranuclear distribution with allosteric responsiveness. Phosphatase competition shows PP1A selectively removes activation-loop phosphorylation while autophosphorylation sites remain protected. This integrated strategy uncovers the proteoform dynamics underlying AMPK activation and provides a broadly applicable framework for studying phosphorylation-based regulation in kinases.

KEYWORDS

Proteoforms, Top-down proteomics, AMPK, Post-translational modifications, FTICR-MS

DATA AVAILABILITY

The mass spectrometry proteomics data generated in this study have been deposited to the ProteomeXchange Consortium via the MassIVE repository with identifier MSV000099446.

ACKNOWLEDGEMENTS

B.K. was supported by the European Union grant 101068151, Top-AMPK, HORIZON-MSCA-2021-PF-01. H.T.R. would like to acknowledge support from the National Heart, Lung, and Blood Institute of the NIH under Award Number T32HL007936 through the UW-Madison Cardiovascular Research Center. C.U. would like to acknowledge funding from the ARIADNE VIBE project, Grant Agreement No. 964553. Y.G. would like to acknowledge NIH R01HL109810 and S10 OD018475 (to Y.G). The author(s) thank the University of Wisconsin Carbone Cancer Center Cancer Informatics Shared Resource, supported by P30 CA014520 for use of its services. All mass spectrometry data reported in this study were acquired at the University of Wisconsin–Madison Human Proteomics Program Mass Spectrometry Facility. We thank Dr. Yanlong Zhu, the facility manager, for expert instrument support and assistance.

AUTHOR CONTRIBUTIONS

Y.G. conceived the study. B.K., C.U., and Y.G. designed the experiments**;** Y.G. supervised the experimental work; B.K., L.B. expressed and purified proteins; B.K. and H-J.C. established and performed phosphorylation assays and MS sample preparation under Y.G.'s direction; H-J.C. acquired FTICR top-down MS fragmentation data; B.K., H.T.R and Z.G. acquired Impact II top-down MS intact data; B.K. and H-J.C. acquired timsTOF bottom-up data; B.K. and H-J.C. analyzed and visualized MS data; B.K. and M.W. performed kinase activity assays; B.K. and S.J.M. calculated total phosphorylation and charge state distribution**.** Y.G. and C.U. supervised the project; B.K., H-J.C, C.U. and Y.G. evaluated results; B.K., H-J.C, C.U. and Y.G. wrote the paper with comments from other co-authors.

CONFLICT OF INTEREST

The authors declare no competing financial interests or conflicts of interest in relation to the work described in this manuscript.

MAIN

Post-translational modifications (PTMs) expand the chemical diversity of the proteome far beyond its genetic blueprint, empowering proteins with the ability to adapt and regulate their functions dynamically[1,2]. Proteoforms, molecular variants of proteins arising from PTMs, alternative splicing, and genetic variation, underpin the functional complexity of biological systems[3–5]. Among the PTMs, phosphorylation creates functionally distinct proteoforms that regulate cellular signaling and metabolic homeostasis[6,7]. Elucidating how multiple phosphorylation sites collectively modulate protein function is essential for developing therapeutics targeting metabolic kinases, which control cellular energy homeostasis and represent promising drug targets for metabolic disorders including diabetes and obesity[8–10]. However, capturing the temporal dynamics and combinatorial patterns of these phosphorylations with analytical precision remains challenging[11,12].

Mass spectrometry (MS)-based proteomics has transformed phosphorylation research by enabling multiplexed, quantitative analysis with sequence-level resolution[13]. Bottom-up proteomics excels at deep proteome coverage and site identification through peptide level analysis, yet it disrupts the proteoforms and loses information on combinatorial modification patterns[14,15]. In contrast, top-down proteomics preserves intact proteoform architectures and combinatorial modification patterns but with limited throughput and difficulty in mapping phosphorylation sites especially for large proteins[16–19] However, achieving both modification specificity and temporal resolution remains challenging. Capturing how individual phosphorylation sites change over time while preserving their combinatorial patterns is critical because phosphorylation can occur in hierarchical cascades in which initial modifications gate subsequent events[20–22]. Experimental strategies must therefore integrate site-specific kinetics with intact proteoform measurements to resolve these dynamic regulatory mechanisms.

Herein, we introduce a hybrid precision mass spectrometry strategy that integrates quantitative intact mass measurements for temporal tracking, bottom-up analysis for site-specific kinetics and top-down sequencing for proteoform characterization. We applied this hybrid strategy to human AMP-activated protein kinase (AMPK), a prototypical system that

exemplifies the analytical challenge of resolving dynamic, multi-site phosphorylation[23,24]. This heterotrimeric complex (α-β-γ) functions as a central regulator of cellular energy metabolism with broad therapeutic relevance across metabolic, cardiovascular, and aging-related diseases [25,26]. AMPK is canonically known to require (i) AMP binding and (ii) activation loop phosphorylation at α1-T183 by upstream kinases such as calcium/calmodulin dependent protein kinase kinase 2 (CaMKK2) to achieve catalytic activation and downstream substrate phosphorylation[27–29]. However, AMPK also undergoes extensive autophosphorylation, creating diverse proteoform landscapes whose regulatory roles and temporal relationships remain poorly defined[28,30].

Using our hybrid precision MS strategy, we uncover AMPK proteoform dynamics during activation, revealing how autophosphorylation creates diverse modification patterns at sites linked to distinct regulatory functions. These findings extend beyond the traditional binary activation model to define a multi-state regulatory paradigm, and establish a generalizable framework for analyzing therapeutic kinase targets.

RESULTS AND DISCUSSION

A Hybrid MS Strategy that enables Dynamic Proteoform Analysis

Our hybrid precision MS strategy integrates three complementary MS approaches to comprehensively characterize phosphorylation dynamics (Fig. 1a-c). (i) Intact protein reverse phase liquid chromatography mass spectrometry (RPLC-MS) quantifies proteoform changes over time (Fig. 1a), (ii) bottom-up MS resolves site-specific phosphorylation kinetics (Fig. 1b), and (iii) top-down fragmentation using ultra high-resolution MS definitively identifies proteoform architectures through sequencing (Fig. 1c). This integrated approach addresses individual method limitations by combining intact mass, sequence information, and temporal dynamics in a single workflow (Fig. 1d).

We applied this strategy to AMP activated protein kinase (AMPK), which exists as 12 possible heterotrimeric combinations through different isoforms (α1-2, β1-2 and γ1-3)[31]. We produced full-length physiological α1β1γ1 isoforms in *E.coli* [32], the ubiquitously expressed

isoform combination in human tissues, and purified the complex to homogeneity (Fig. 1e-f, Table S1). We activate AMPK using AMP and CaMKK2 mediated phosphorylation (Fig. 1g). AMPK functionality was validated through activity assays using synthetic SAMS peptide substrate which confirmed that the enzyme was functional with an EC50 of 7.8 ng, demonstrating quality comparable to commercial preparations (Fig. 1h)[33]. Time-resolved phosphorylation reactions were performed and were quenched at defined intervals for MS analysis (Fig. 1i).

AMPK Subunits Exhibit Distinct Phosphorylation Hierarchies

AMPK subunits undergo differential phosphorylation with distinct temporal patterns. To quantify these dynamics, we performed *in vitro* phosphorylation of the AMPK complex using CaMKK2/Calmodulin. CaMKK2 represents a primary upstream kinase of AMPK, phosphorylating α1-T183 in the activation loop, resulting in about 100-fold activity enhancement[27]. To analyze phosphorylation status, we applied intact protein RPLC-MS approach, providing highly reproducible chromatographic separation (Fig. 2a). Intact mass analysis of unphosphorylated AMPK subunits confirmed the expected molecular weights (Table S2).

Intact protein MS at the initial time point showed well-resolved charge state distributions (Fig. 2b, Fig. S1a). Deconvoluted mass analysis confirmed proteoform identification with high mass accuracy (Fig. 2c). Although we detected initial phosphorylation and mass heterogeneity through non-specific modifications known from *E.coli*[34] (Fig. 2d), the unmodified mass species (0P) was by far the dominant form in all three subunits prior to CaMKK2 treatment, after which phosphorylation levels increased dramatically (Fig. 2e). Analysis of total phosphorylation (P_{total}) over 200 min revealed the sequential mass increase across AMPK subunits, culminating in the highest levels for α1 (5.33±0.04), intermediate for β1 (2.72±0.01), and minimal for γ1 (0.61±0.01) (Fig. 2f, extended validation in Fig. S1b).

Representative deconvoluted mass spectra across the time course demonstrate the sequential phosphorylation events (Fig. 2f). The maximum phosphorylation states observed at

200 min (α1: 7P, β1: 4P, γ1: 1P) represent the minimum number of phosphorylatable sites on each subunit, since not all sites reach full stoichiometric phosphorylation. Distribution of AMPK proteoforms throughout the spectra revealed distinct phosphorylation behaviors: α1 exhibited a broad, distributed envelope indicating multiple competing modification pathways, while β1 showed preferential accumulation at the P2 state, suggesting a more channeled phosphorylation pattern with one predominant proteoform.

While numerous phosphorylation sites have been reported for AMPK subunits, our results reveal richer phosphorylation patterns than expected from direct CaMKK2 targeting alone, most likely stemming from triggered autophosphorylation cascades following initial α1-T183 activation[30,35–40]. MS- based and biochemical studies report variable numbers of potential autophosphorylation sites (approximately 6 for α1, 7 for β1, none for γ1 based on PhosphoSitePlus compilation), the specific sites and stoichiometry depend heavily on experimental conditions[41]. These quantitative phosphorylation profiles revealed distinct subunit-specific hierarchies, motivating investigation of the underlying regulatory mechanisms driving AMPK activation.

Phosphatase Competition Reveals Selective Targeting of Activation Sites

AMPK regulation involves a dynamic equilibrium between kinase-mediated phosphorylation and phosphatase-mediated dephosphorylation, with protein phosphatases such as PP1A preventing constitutive activation[42]. We investigated the interplay through competitive phosphorylation-dephosphorylation reactions using increased PP1A concentrations. In the absence of PP1A, total phosphorylation after 100 min reached levels (α1: 4.44 ± 0.03P, β1: 2.34 ± 0.01P, γ1: 0.46 ± 0.01P) (Fig. 3a, Fig. S2a-c), which are comparable to the previous experiments. However, even low PP1A (4.52 μM) concentrations selectively reduced α1 phosphorylation by approximately 1 P (~0.93 P decrease), while β1 (~0.18 P decrease) and γ1 levels (decrease within error) remained relatively stable (Fig. 3b). Even at high PP1A concentrations, substantial phosphorylation persisted, indicating that PP1A selectively removes the activating phosphorylation at T183 on the α1 subunit, whereas

autophosphorylation sites appear protected from dephosphorylation, underscoring these modifications are kinetically stable once established (Fig. 3c).

Site-Directed Mutagenesis Defines CaMKK2 Specificity

To investigate the connection between CaMKK2 and extensive AMPK phosphorylation patterns, we employed site-directed mutagenesis. We generated two activity-deficient AMPK mutants: α1-T183A, which cannot be phosphorylated at the activation loop, and α1-K56N, a catalytically dead mutant (Fig. 3d, Fig. S3a). RPLC-MS analysis revealed striking differences in CaMKK2-mediated modification patterns (Fig. 3e). Wild-type AMPK exhibited phosphorylation levels as observed in previous experiments, whereas the α1-T183A mutant showed virtually no detectable phosphorylation on either subunit.

Most revealing was the catalytically dead K56N mutant, which showed exactly one phosphorylation on α1 and none on β1 (Fig. S3b). This single modification at α1-T183 is the sole direct CaMKK2 target, establishing that all other phosphorylations arise from subsequent autophosphorylation (Fig. 3f). Having established this canonical activation mechanism, we next investigated whether alternative activation mechanisms could similarly trigger autophosphorylation cascades.

Allosteric Activation Bypasses Canonical Phosphorylation Requirements

AMPK contains an allosteric drug and metabolite (ADaM) binding site located at the interface between the α-kinase domain and β-subunit, which can be activated by small molecules, enhancing activity up to 10-fold[43]. We employed PF-739, a small molecule ADaM site activator, demonstrating dose-dependent AMPK activation with 3.8-fold enhancement over AMP alone (Fig. 3g-i).[44]

Most significantly, while AMP alone produced minimal phosphorylation in both wild-type and T183A AMPK, addition of PF-739 resulted in substantial phosphorylation (α1: 4.63 ± 0.12P, β1: 1.79 ± 0.01P, respectively) (Fig. 3j, Fig. S3c, comparable to CaMKK2 activation levels. These findings demonstrate that allosteric activation by PF-739 enables robust autophosphorylation even in T183A mutants, supporting a model where PF-739 binding

promotes a catalytically competent state independent of activation loop phosphorylation (Fig. 3k, S4a)[45].

Site-Specific Phosphorylation Kinetics Reveal Mechanistic Hierarchy

To identify specific sites causing the observed phosphorylation hierarchy, we employed bottom-up MS using identical aliquots from the CaMKK2-AMPK reaction samples (Fig. 4a, Fig. S5b-d). Phosphorylation kinetics were quantified by monitoring extracted ion chromatograms (EIC) peak areas over time for peptide pairs that showed inversely correlating behavior (Fig. 4b-c, Table S3-5, Fig. S5a). Sixteen peptide pairs met these criteria and were used to generate kinetic profiles, revealing the phosphorylation dynamics with detailed temporal and site-specific detail (Fig. 4d).

Phosphorylation kinetics were determined from unphosphorylated peptide disappearance (normalized to initial values), as this provides the most reliable measure of modification progression independent of differential ionization efficiencies between modified and unmodified forms. Our analysis revealed striking differences in phosphorylation rates and extents across AMPK sites, establishing a quantitative hierarchy of modification events (Fig. 4e-f). The most rapid autophosphorylation occurred at α1-S496, a site associated with inhibitory regulation[46], exhibiting an exceptionally high kinetic rate (0.16 ± 0.05 min^{-1}) and complete phosphorylation within 25 min. This reflects efficient trans-autophosphorylation by the CaMKK2-activated population, which phosphorylates S496 on neighboring AMPK molecules faster than CaMKK2 phosphorylates α1-T183 (0.077 ± 0.005 min^{-1}).

The well-characterized phosphorylation site β1-S108, often cited as AMPK's prototypical autophosphorylation site due to its role in facilitating allosteric activation at the ADaM site, showed excellent kinetic behavior (R^2 = 0.99) with complete modification by 50 minutes, representing the faster end of well-studied sites[47]. While β1-T148 exhibited a higher rate constant (0.077 ± 0.083 min^{-1}) than S108, this regulatory site crucial for glycogen binding demonstrated moderate phosphorylation extent (0.45) and quantification challenges arising from the complex peptide sequence (FFVDGQWTHDPSEPIVTSQLGpTVNNIIQVK), making

kinetic parameter interpretation less reliable[48]. This kinetic analysis established distinct rate categories, enabling discrimination between rapid primary regulatory events and slower secondary modifications.

Beyond these well-characterized sites, several sites displayed moderate kinetics, including α1-S176 (0.053 ± 0.014 min^{-1}, extent = 0.62) and γ1-S9 (0.055 ± 0.027 min^{-1}, extent = 0.80), which showed substantial phosphorylation extents suggesting some genuine regulatory roles. However, sites with very slow phosphorylation kinetics like α1-T388 (0.007 ± 0.004 min^{-1}, extent = 0.35) or minimal modification like α1-S136 (0.071 ± 0.15 min^{-1}, extent = 0.09) likely represent secondary regulatory mechanisms or sites irrelevant *in vivo*.

Among the analytical challenges was quantification of convoluted phosphorylations at the α1 C-terminus regulatory sites. However, a shorter 23-residue peptide from semi-specific trypsin cleavage (SSEVSLTSSVTSLDSSPVDLTPR/P) separated into three distinct chromatographic peaks corresponding to phosphorylation at α1-S516, α1-S524, and α1-T526 (Fig. S5e). The unphosphorylated parent peptide decreased slowly (k = 0.008 ± 0.008 min^{-1}) but achieved high phosphorylation extent of 0.81. The total phosphorylation is distributed across the three sites, which accumulated with comparable chromatographic intensities, indicating all three positions within the α-subunit's C-terminal regulatory domain are accessible for modification.

The close correlation between peptide-level and intact protein quantification validates our integrated strategy, though systematic discrepancies reveal the complementary nature of each method. The α1 and β1 subunit difference (4.6P vs. 5.3P, 2.0P vs. 2.7P, respectively) suggests the presence of modifications not captured by bottom-up analysis. These discrepancies, rather than representing limitations, highlight the necessity of direct proteoform characterization to definitively identify modification combinations that remain masked in peptide-based approaches.

Our site-specific kinetic analysis provides detailed mechanistic insight, revealing that AMPK autophosphorylation involves a complex hierarchy of sites with distinct kinetic properties However, while bottom-up analysis identified individual phosphorylation sites, the specific combinations of modifications within intact proteoforms remained unresolved.

Top-Down Sequencing Validates Proteoform Architecture

To characterize proteoform architecture and validate quantitative measurements, we employed ultrahigh resolution (>400,000 at 400 *m/z*) Ultra high-resolution MS top-down sequencing analysis. Direct Nano-ESI of denatured AMPK subunits yielded high-quality spectra with isotopic resolution. However, the α1 subunit showed strong signal suppression due to size-related effects and was only detectable in the unphosphorylated control sample. In contrast, the smaller β1 and γ1 subunits dominated the signal response in both conditions (Fig. 5a, Fig. S6a-b).

Examination of β1 intact mass spectra from the CaMKK2-treated sample revealed heterogeneous phosphorylated species (1P-7P), with doubly phosphorylated (2P) as the major component (Fig. 5b). Top-down measurements showed total β1 phosphorylation of 3.1P, slightly higher than our earlier RPLC-TOF analysis (2.7P), likely due to different ionization conditions. Summing phosphorylation extents from all identified peptides in bottom-up analysis yielded only 2.0P, revealing a 0.7-1.1P discrepancy compared to intact protein measurements. This missing phosphorylation made the predominant 2P β1 ideal for structural characterization to identify undetected modification sites. Quadrupole isolation of the 2P β1 23+ precursor (1323 *m/z*) achieved mass species selectivity with high mass accuracy (1.9 ppm) (Fig. 5c-d).

Comprehensive structural characterization was performed using complementary fragmentation approaches combining collision-induced dissociation (CID) and electron capture dissociation (ECD) at optimized parameters (Fig. 5e, Fig. S7). Data processing utilized our in-house MASH software with eTHRASH deconvolution algorithm for automated peak detection, followed by mass-based fragment assignments to theoretical ion envelopes and manual curation for all assignments.[49] The combined fragmentation experiments yielded 179 high-

confidence fragment ions (43 b-, 54 c-, 34 y-, 48 z-type) across the 269-residue β1 sequence, achieving 54% backbone coverage and high mass precision (Figure 5f-g). Systematic fragment analysis revealed the major bis-phosphorylated proteoform (2P) carries phosphorylation at S24/25 and S108.

The first phosphorylation was localized to the S24/25 double serine motif based on c^{22}, c^{23}, and c^{24} fragment ions. Quantitative analysis of unphosphorylated and mono-phosphorylated fragment pairs demonstrated predominant phosphorylation at S24 compared to S25 (60% vs 16%) (Fig. S8), consistent with the mutually exclusive phosphorylation pattern described for this site[39]. While not universally applicable for double serine motifs, the autophosphorylation of either S24 or S25 appears to preclude modification of the adjacent site due to altered kinase recognition specificity[50,51]. The identification of S24/25 phosphorylation directly addresses the quantitative discrepancy between intact protein and peptide-level measurements. This site was absent from bottom-up analysis due to poor N-terminal coverage; the 6-residue tryptic peptide DSSGTK containing S24/S25 was not detected.

The second phosphorylation site, S108, was definitively assigned based on 27 high-confidence fragment ions spanning this region. This S24/25+S108 combination represents a notable finding, as S24/25 phosphorylation has been linked to extranuclear distribution, while S108 phosphorylation facilitates allosteric activation by stabilizing the ADaM site binding pocket[37,52]. Such combinatorial modification on a single β1 proteoform could functionally tether subcellular localization signals with allosteric responsiveness, creating an integrated regulatory mechanism. The strong predominance of the 2P species in intact mass spectra, combined with the consistent identification of this specific S24/25+S108 combination, suggests a channeled phosphorylation pathway rather than stochastic modification of available sites. Notably, β1-S101 and β1-T148 phosphorylation could not be detected in our top-down analysis, despite identification in bottom-up experiments, indicating these represent minor proteoforms under these experimental conditions. Our ultra-high-resolution MS analysis thus provides definitive

structural validation of the complex proteoform architectures revealed by our integrated analytical approach.

Mechanistic Model and Structural Mapping of AMPK Phospho-Proteoforms

Our comprehensive analysis creates a model for AMPK proteoform regulation based on four key mechanisms (Fig. 6a): (1) The main activation pathway through T183 phosphorylation by CaMKK2 can be alternatively circumvented through allosteric activation that can directly enable autophosphorylation. (2) This connects to a dual phosphorylation cascade where both CaMKK2-mediated α1-T183 phosphorylation and direct allosteric activation trigger extensive autophosphorylation across all subunits following distinct kinetic hierarchies, with α1-S496 showing the highest kinetic efficiency. (3) The model incorporates channeled proteoforms through coordinated modifications, exemplified by the prevalent β1 S24/25 + S108 combination, tethering functionally relevant phosphorylation sites. (4) Finally, persistent autophosphorylation occurs because while PP1A removes activity through T183 dephosphorylation, autophosphorylation sites remain largely protected, suggesting that these sites modifications could persist until protein turnover in the absence of other phosphatases.

Our structural analysis revealed that identified phosphorylation sites cluster into four distinct hotspots (Fig. 6b-c) corresponding to key functional regions. The activation sites and catalytic center (Fig. 6d) contain the phosphosites α1-T183, α1-S176, and β1-S108, where α1-T183 and β1-S108 are directly responsible for main and allosteric activation, while nearby α1-S176 potentially influences catalytic function. The α1 Serine-Threonine-rich loop (ST-loop) (Fig. 6e) encompasses S496, S524, S516, and T526 phosphorylations, orchestrating negative feedback by reducing α1-T183 phosphorylation through electrostatic interactions with basic residues near the active site[46,53]. The α1-auto-inhibitory domain (AID) and α-hook region (Fig. 6f) represents a regulatory hub containing phosphorylations at T388, S397, S360, S356, and T355[54]. The β1 carbohydrate-binding module (Fig. 6g) features the well-characterized T148 phosphorylation mediating AMPK sequestration at glycogen, alongside structurally proximate S96 and S101 requiring further investigation[48]. This spatial organization reveals how AMPK integrates multiple regulatory inputs through autophosphorylation cascades that create

proteoform diversity, extending beyond a binary activation model to enable fine-tuned kinase regulation.

CONCLUSION

Our integrated mass spectrometry approach quantitatively resolves AMPK proteoform dynamics with high precision, revealing temporal hierarchies and regulatory mechanisms previously obscured by single-method analysis. The combination of intact mass measurements, site-specific kinetics, and top-down sequencing captures combinatorial modification patterns and kinetic relationships that extend beyond the traditional binary activation model. Rather than α1-T183 phosphorylation serving as a simple on/off switch, initial activation triggers diverse autophosphorylation cascades that generate proteoform populations with distinct modification patterns at functionally characterized sites. Additionally, selective phosphatase resistance of autophosphorylation sites reveals temporal persistence distinct from canonical activation loop regulation.

The intact protein mass approach proved exceptionally valuable for interrogating biochemical mechanisms using accessible instrumentation, while temporal dynamics provided mechanistic insights that fundamentally shift our understanding of how these phosphorylations occur and function. Bottom-up analysis defined kinetic rate constants for individual sites, and top-down sequencing identified a channeled doubly phosphorylated β1 proteoform. Where previous studies revealed AMPK's structural heterogeneity[55] and phosphorylation site diversity[56], our integrated approach now resolves the temporal mechanisms and kinetic hierarchies that generate these proteoform populations. Discrepancies between methods exposed analytical biases inherent to single approaches, validating the necessity of this integrated strategy.

This hybrid analytical platform extends beyond AMPK, providing a generalizable framework for characterizing therapeutic kinase targets where proteoform-specific regulation remains poorly understood. The approach enables dissection of kinase activation mechanisms

with temporal and modification-state precision, informing development of therapeutics that target specific regulatory states rather than global kinase inhibition.

METHODS

Genes and Protein Constructs

Recombinant protein sequences were based on UniProt entries human AMPK alpha1 (Q13131), beta1 (Q9Y478), and gamma1 (P54619). The expression plasmid pET28-H6-AMPKγ1β1α1 for AMPK full-length, with His tag (MSYYHHHHHHEGVRTM-) N-terminally fused to the alpha subunit, and pET24 H6GST-hPP1Aα (aa1-314, PP1A domain) was generated by Karsten Melcher Lab and kindly provided by Van Andel Institute. Site-directed mutations on AMPK alpha K56N and T183A were introduced using the Q5 site-directed mutagenesis kit (New England Biolabs) and confirmed using long-read DNA sequencing (UW-Madison Biotechnology Center).

Expression and Purification

AMPK and PP1Aα were produced as recombinant proteins in One Shot BL21 Star (DE3) E. coli (Thermo Fisher). Cells were grown in 1 L baffled flasks to OD_{600} = 0.8-1.0, induced with 0.1 M IPTG, and continued at 18°C for 20 h. Cell pellets were lysed in His equilibration buffer (20 mM imidazole, 40 mM phosphate, 300 mM NaCl, pH 8) by sonication. His-tagged proteins were purified using HisPur Ni-NTA resin (Thermo Fisher) with sequential washes (50 mM imidazole) and elution (300 mM imidazole). Proteins were buffer-exchanged into storage buffer (20 mM phosphate, 150 mM NaCl, 300 mM imidazole, 15% glycerol, 2 mM DTT), concentrated to 5-10 mg/mL, and stored at -80°C. Concentrations were determined by Bradford assay (BioRad) or NanoDrop (Thermo Scientific). CaMKK2 (CaMKK beta isoform 2 [1 – 541]) was obtained through the MRC PPU Reagents and Services facility (MRC PPU, College of Life Sciences, University of Dundee, Scotland):

AMPK Phosphorylation Reactions

All reactions were performed in assay buffer (50 mM HEPES, 100 mM NaCl, 2 mM DTT, 0.01% Brij 35). CaMKK2 was premixed with calmodulin (Enzo Life Sciences) at a 1:2 molar ratio. For phosphorylation, 7.5 μM AMPK was incubated with 0.155 μM CaMKK2 and 0.31 μM calmodulin in the presence of 500 μM ATP, 200 μM AMP, 5 mM $(CH_3COO)_2Mg$, and 1 mM $CaCl_2$ at 20°C for up to 200 min in [240 μL total volume]. Aliquots (~15 μg protein) were

quenched at defined intervals with 0.1% formic acid. For concentration-dependent PP1A phosphatase experiments, PP1A was added at varying concentrations to CaMKK2 AMPK mixtures, and samples were quenched after 200 min.

Quenched reactions were desalted using chloroform-methanol-water precipitation. AMPK was diluted into 400 µL water, precipitated with 400 µL methanol, phase-separated with 100 µL chloroform, and centrifuged at 15,000 g for 10 min. Following supernatant removal, 400 µL methanol was added and mixed by rocking. After centrifugation, proteins were further desalted by two consecutive methanol washes. Air-dried pellets were stored at -80°C until analysis.

Intact LC-MS Analysis

Desalted reaction samples were reconstituted in 5% FA/20% acetonitrile-isopropanol and adjusted to 200 ng/µL. LC-MS was performed using nanoAcquity UPLC (Waters) coupled to Impact II Quadrupole Time-Of-Flight (QTOF) (Bruker Daltonics). Samples (300-500 ng) were separated on a home-packed C4 column (Halo, 2.7-µm, 250-µm ID, 1,000 Å) using gradient: 0-3 min, 10% B; 3-20 min, 10-80% B; 20-24 min, 80-95% B; 24-30 min, 95%-10% B (A: 0.1% FA in H_2O; B: 0.1% FA in acetonitrile) at 4 µL/min.

Mass spectra were acquired at 0.5 Hz over 300-3000 m/z. Source parameters: capillary voltage 4500 V, nebulizer pressure 0.5 bar, dry gas 4.0 L/min at 200°C. Ion transfer settings: funnel RF 300 V, quadrupole energy 5 V, low mass cutoff 650 m/z, isCID 10 V, collision RF 2600 Vpp.

Data processing used Compass Data Analysis (Bruker). Summed mass spectra were generated from fixed time windows. Deconvolution employed MaxEnt with different parameters for isotopic resolved (β/γ: resolution 40,000) versus non-resolved (α: resolution 10,000) charge envelopes. Spectra were smoothed (Savitzky-Golay 0.2), background subtracted (0.55), and peak-picked. Peak lists were manually curated for phosphorylation masses and exported for weighted average calculations. The total weighted phosphorylation average was calculated by the following formula:

$$\frac{(P0*0+P1*1+\cdots*Pi*i)}{(P0+P1+\ldots+Pi)} = p_{total}$$

Bottom-up MS Analysis

Desalted reaction samples were reconstituted and neutralized with ammonium bicarbonate (pH 8), before being reduced with 10 mM TCEP (37°C, 30 min), alkylated with 500 mM chloroacetamide (RT, 30 min), and digested with trypsin (37°C, overnight). Peptides were desalted using C18 stage tips and analyzed by LC-MS/MS.

Samples (200 ng) were separated on Ion Optics columns (25 cm × 75 µm, C18 1.6 µm) at 55°C using 50 min gradients (2-37% B, then 37-85% B over 5 min; A: 0.2% FA in water, B: 0.2% FA in ACN) at 400 nL/min. Analysis used Trapped Ion Mobility Spectrometry (tims)-TOF Pro (Bruker) in PASEF mode with ion mobility 0.60-1.60 Vs/cm² and standard fragmentation parameters (10 MS/MS scans, 1.17 s cycle time, 20-59 eV collision energy).

Data were processed in Skyline (v23.1.0.380) to extract peak areas (area under the curve, AUC) from corresponding phosphorylated/unphosphorylated peptide pairs. Peak areas were normalized to the maximum value within each peptide series and analyzed in GraphPad Prism. Unphosphorylated peptides were fit to one-phase decay models to obtain rate constants (k, min^{-1}), while phosphorylated peptides were fit to one-phase association models for validation. Phosphorylation extent was calculated as $(AUC_{max} - AUC_{min})/AUC_{max}$ from the normalized peak areas, representing the fraction of peptide phosphorylated. Only peptide pairs showing inverse correlation were included in the final analysis.

Top-down MS

Phosphorylated AMPK samples were analyzed using solariX XR 12T Fourier-Transform Ion Cyclotron Resonance (FTICR) mass spectrometer (Bruker) coupled to TriVersa Nanomate (Advion). NanoESI conditions: 0.45 PSI desolvating gas pressure, 1.5-1.55 kV voltage, 3 L/min dry gas at 180°C. Source optics were optimized: capillary exit 240 V, detector plate 220 V, funnel 1 at 150 V, skimmer 50 V, funnel RF 300 Vpp, octopole frequency 5 MHz with 600 Vpp RF, collision cell at 2 MHz with 2000 Vpp RF.

Mass spectra were acquired with 2M data points over 200-4000 m/z range. Precursor isolation used ≥4 m/z windows. Collision-activated dissociation (CAD) employed 12-35 V collision energy. Electron capture dissociation (ECD) parameters: pulse length 0.01-0.03 s, bias 0.5-1.5 V, lens voltage 5-15 V. Fragment ion assignments were performed using standard top-down proteomics approaches for proteoform characterization. MS2 data were analyzed using MASH Native for proteoform sequencing and PTM localization[49]. Fragments were identified using eTHRASH algorithm. All fragments were manually validated.

Data Integration and Analysis

Intact protein phosphorylation levels were quantified from deconvoluted mass spectra using weighted averages. Site-specific extent from bottom-up analysis were correlated with total phosphorylation measurements. FTICR MS2 data provided definitive proteoform identification and phosphosite localization and used for complementing the results.

FIGURES AND CAPTIONS

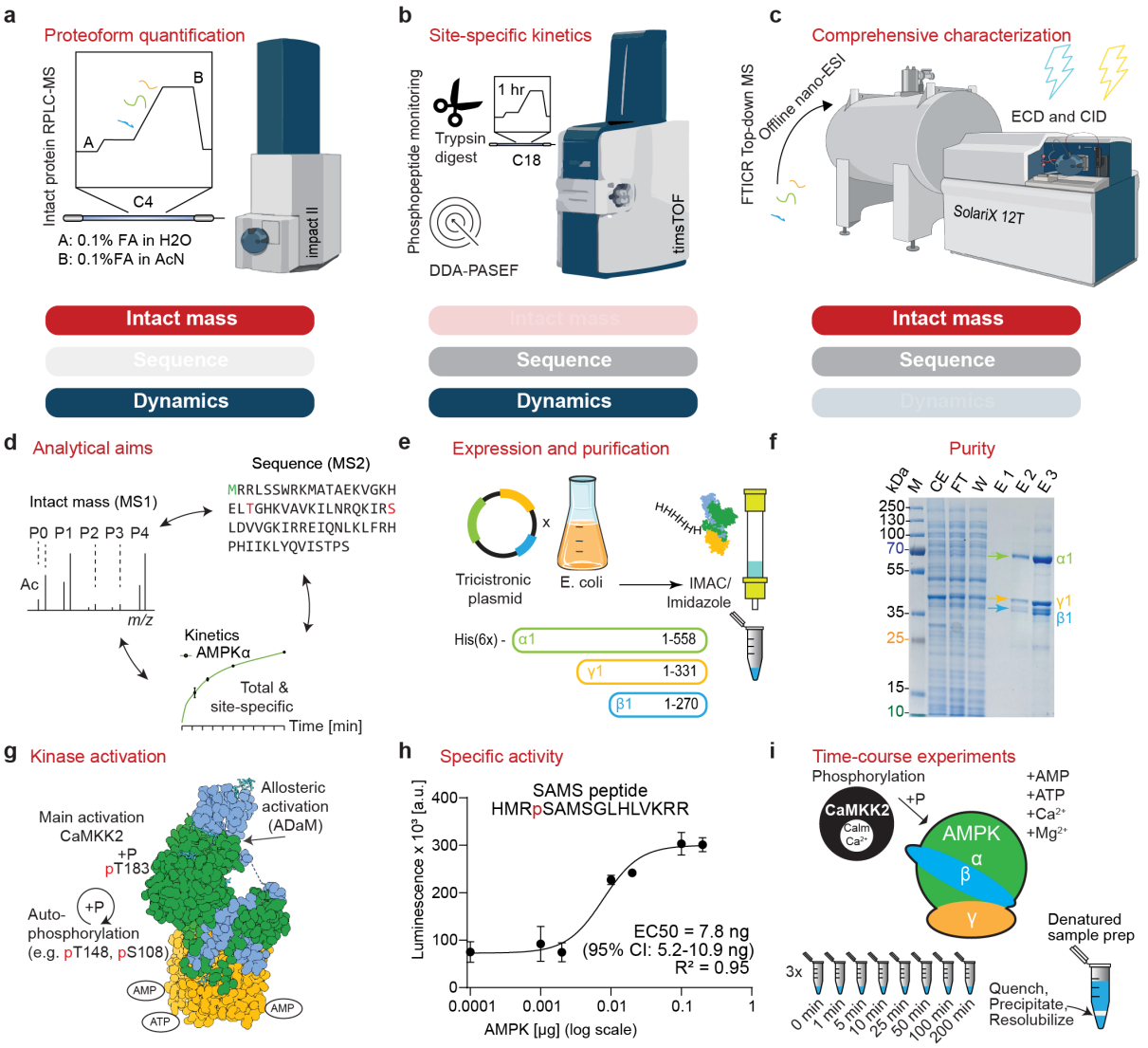

Figure 1: Hybrid mass spectrometry-strategy for comprehensive kinase phosphorylation analysis. (a) Intact proteoform tracking via LC-MS (C4 RPLC coupled to MS). **(b)** Site-specific phosphorylation kinetics via bottom-up MS. **(c)** Top-down proteoform characterization using ultra high-resolution MS with various fragmentation options. **(d)** Conceptual integration of the three approaches to capture intact mass, sequence information, and temporal dynamics. **(e)** Heterologous AMPK expression and affinity purification workflow. **(f)** SDS-PAGE analysis confirming purity of affinity purified AMPK complex with approximately stoichiometric subunit ratios. **(g)** AMPK activation mechanism: AMP binding promotes CaMKK2-mediated T183 phosphorylation and subsequent autophosphorylation cascade. **(h)** Validation of enzyme activity using SAMS peptide substrate showing dose dependent

response (*n=3*). AMPK concentration on logarithmic scale. **(i)** Time-course phosphorylation workflow: AMPK incubated with CaMKK2 and cofactors, with samples quenched at defined intervals and prepared by chloroform methanol water precipitation.

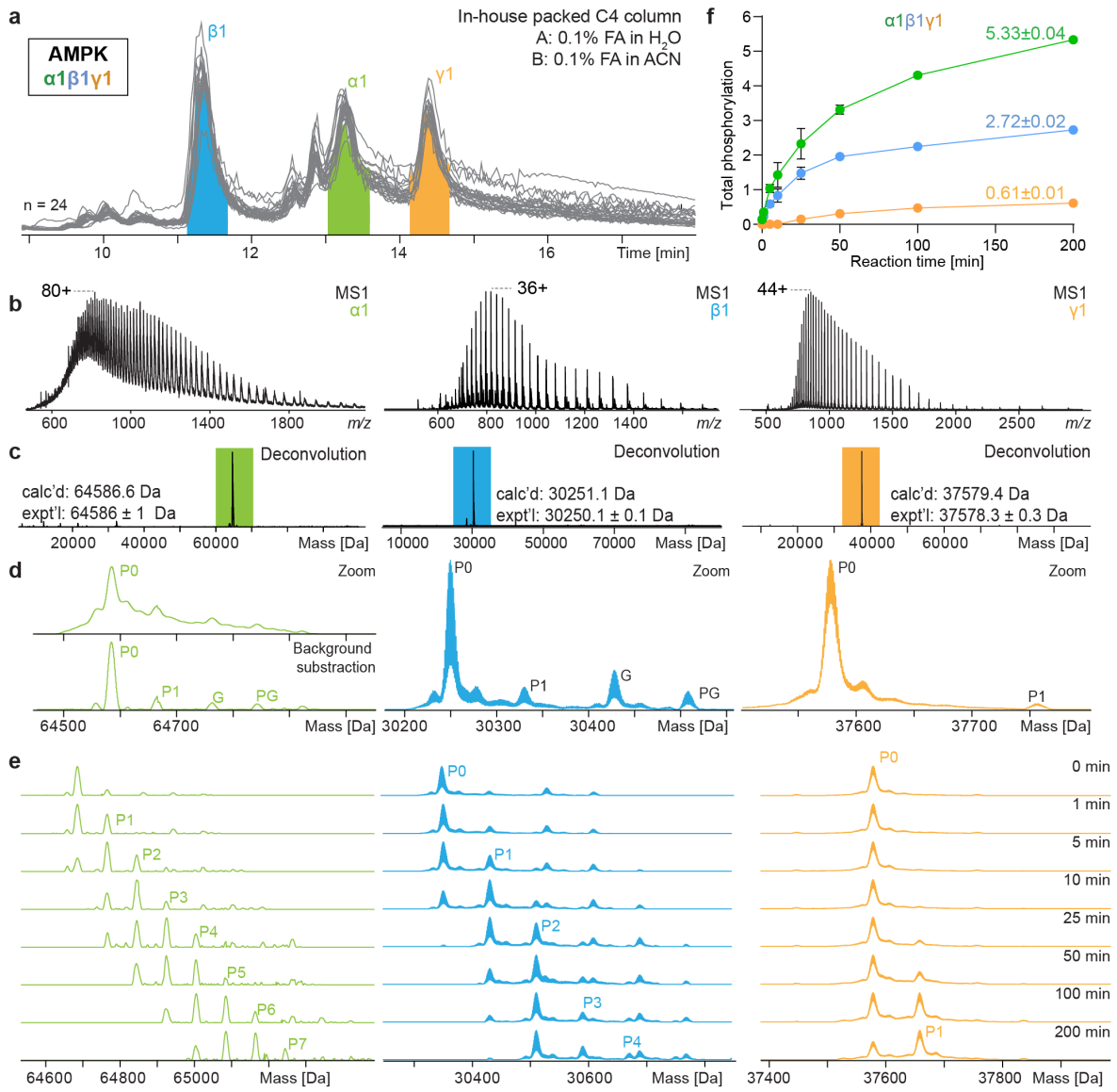

Figure 2: AMPK proteoform quantification by intact protein RPLC-MS during CaMKK2-mediated activation. (a) Total ion chromatograms of 24 consecutive runs across the phosphorylation time course. **(b)** Graph of total phosphorylation dynamics with error bars representing mean ± SEM (*n=3*) determined over 200 min. **(c)** MS1 intact protein spectra at 0 min reaction time with most abundant charge states labeled. **(d)** Deconvoluted mass spectra for proteoform identification showing calculated (calc'd) and experimental (expt'l) masses.

Mass differences of ~1 Da between experimental and calculated values commonly result from isotopologue selection during deconvolution. **(e)** Quantifiable peaks labeled with their corresponding proteoforms. P = Phosphorylation, G = Gluconoylation, PG = Phosphogluconoylation. **(f)** Representative deconvoluted mass spectra showing temporal progression of mass increases corresponding to sequential phosphorylation events.

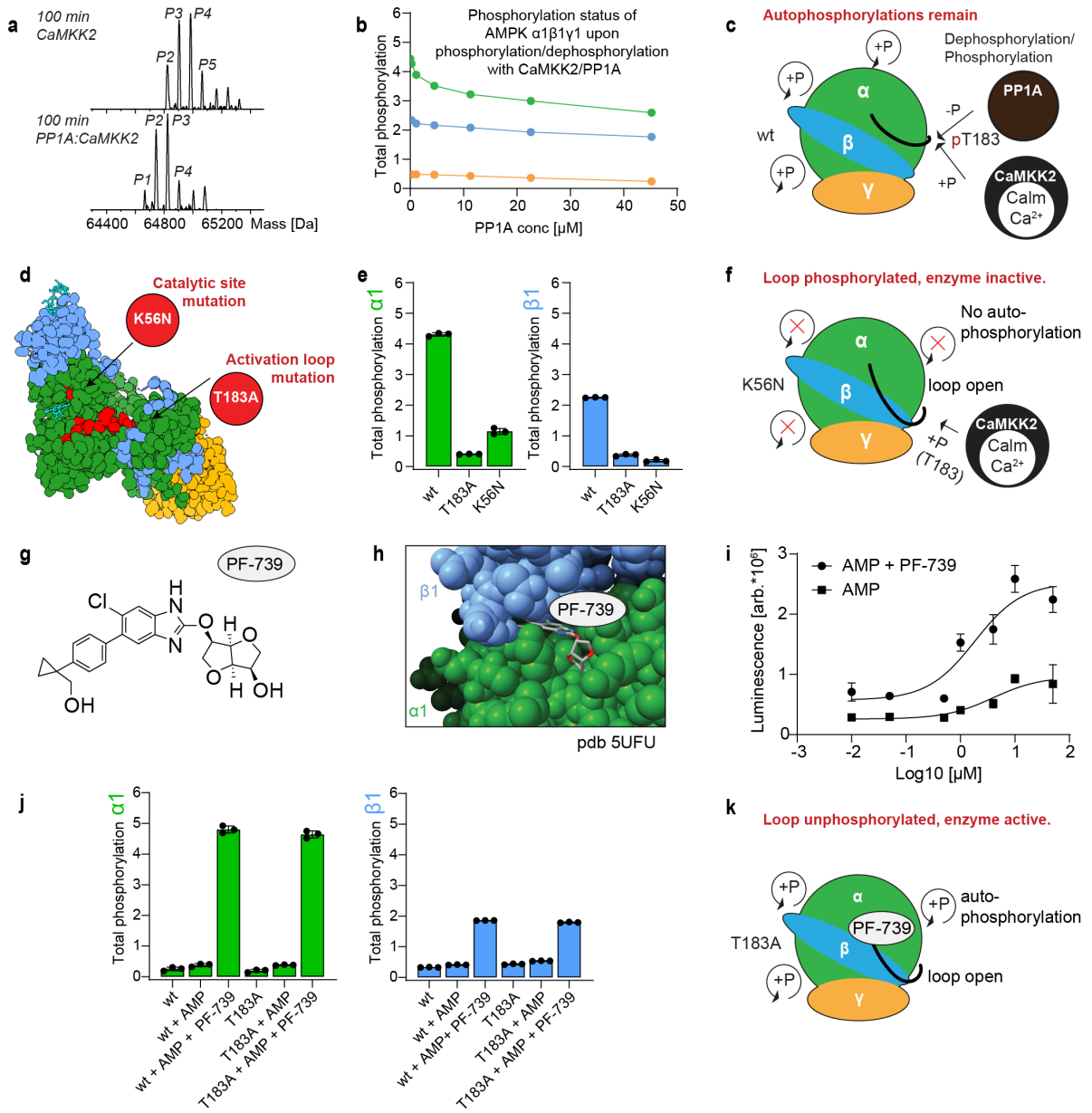

Figure 3: Deciphering AMPK mechanisms. (a) MS1 intact protein spectra show that the total phosphorylation of AMPK α1 decreases (~1P) upon phosphatase addition. **(b)** Concentration-dependent total phosphorylation-dephosphorylation dynamics with error bars representing

mean ± SEM (*n=3*), AMPK α1 decreases earlier and more than β1 and γ1 subunit. **(c)** Schematic showing the phosphorylation/dephosphorylation of AMPK by CaMKK2 and PP1A, respectively. **(d)** Structural model showing site-directed mutations: catalytic site (K56N) and activation loop (T183A). **(e)** Total phosphorylation quantification in WT and mutants following CaMKK2 treatment (mean ± SEM, *n=3*), T183A is invariant upon CaMKK2 addition while K56N increases selectively (~1 P) in α1 subunit. **(f)** CaMKK2-mediated activation loop phosphorylation in catalytically inactive K56N mutant. **(g-h)** PF-739 structure and ADaM site binding location. **(i)** ADP-Glo kinase assay showing dose-dependent allosteric activation (arbitrary units, mean ± SEM, *n=3*). Peak activation showing 3.8-fold enhancement over AMP alone. **(j)** Phosphorylation analysis of WT and T183A AMPK following allosteric activation; wt and T183A show intense phosphorylation by allosteric activation, indicating that the T183 phosphorylation is circumvented. **(k)** PF-739-mediated enzyme activation despite unphosphorylated activation loop.

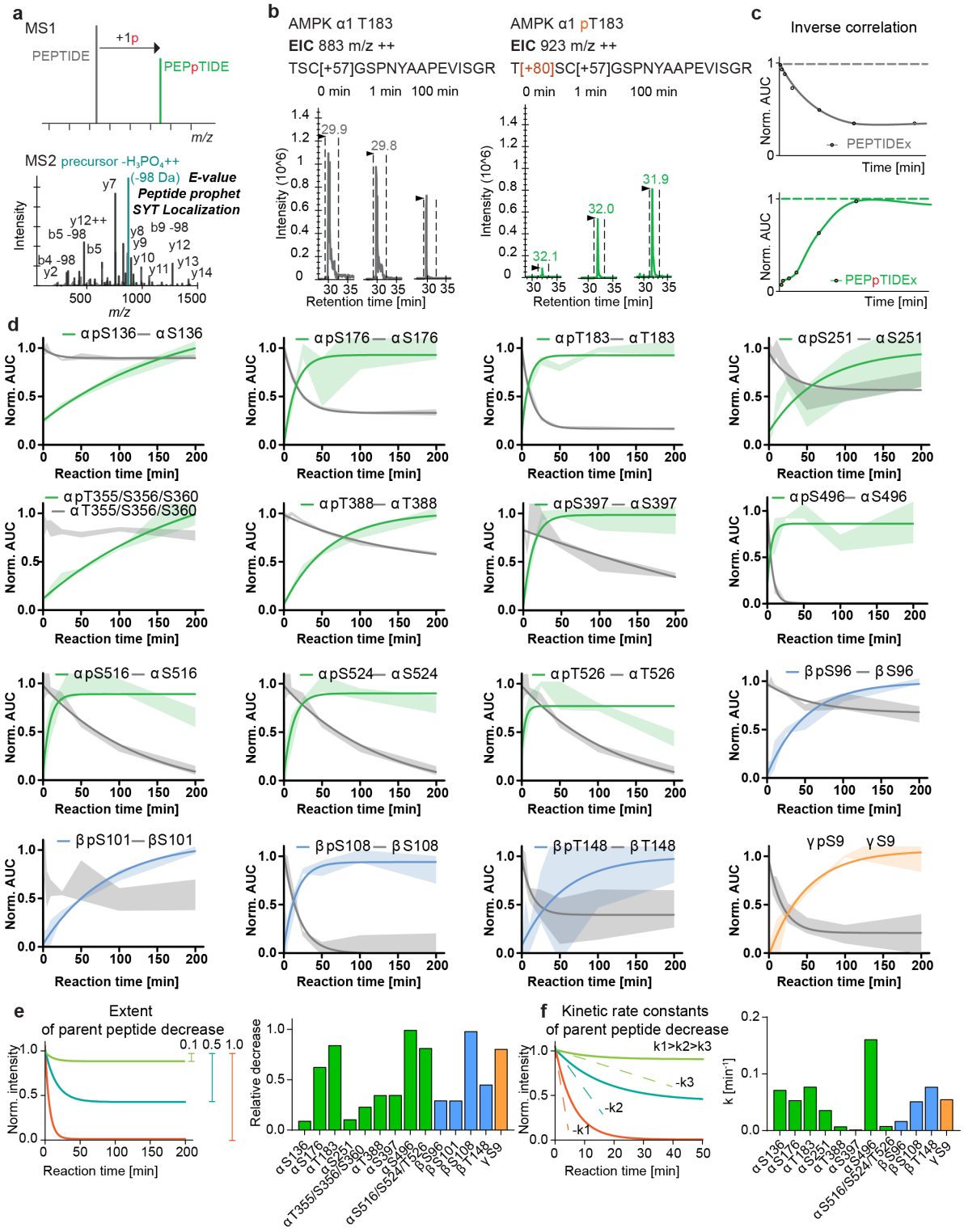

Figure 4: Site-specific phosphorylation kinetics reveal mechanistic hierarchy using bottom-up MS. (a) Phosphorylated/unphosphorylated peptide pair tracking and MS2 spectrum showing spectral quality and localization confidence for phosphopeptide validation. **(b)** Temporal progression at 0, 1, and 100 min for parent peptide and phosphopeptide T183 showing inversely correlating intensities. **(c)** Schematic of kinetic plots with inversely

correlating changes over time monitored as Normalized Area Under Curve (AUC). **(d)** Site-specific phosphorylation kinetics for 16 peptide pairs with color-coded subunit assignment (α1: green, β1: blue, γ1: yellow-orange). One-phase decay curve fitting applied. Shaded bands represent mean ± SEM. **Note**: S516, S524 and T526 have the same parent peptide. Parent peptides of α1 T355/T356/S360 and β1 S101 could not be fit with the one-phase decay model. **(e)** Schematic showing how extents of phosphorylation were determined from parent peptide decrease; bar graph showing extents of phosphorylation. **(f)** Schematic showing how kinetic rate constants (k) were obtained by fitting peptide disappearance curves to a one-phase decay model. **Note**: Parent peptides for β1 S101 and α1 S397 showed early-timepoint variability within the first 10 min, could not be fit to the one-phase decay model and were only analyzed for their extent. The α1 S397 quantification challenges likely arise from (1) the peptide containing one missed cleavage site, complicating accurate quantification, and (2) sequence overlap with the T388-containing peptide, where T388 phosphorylation also decreases the S397 parent peptide intensity.

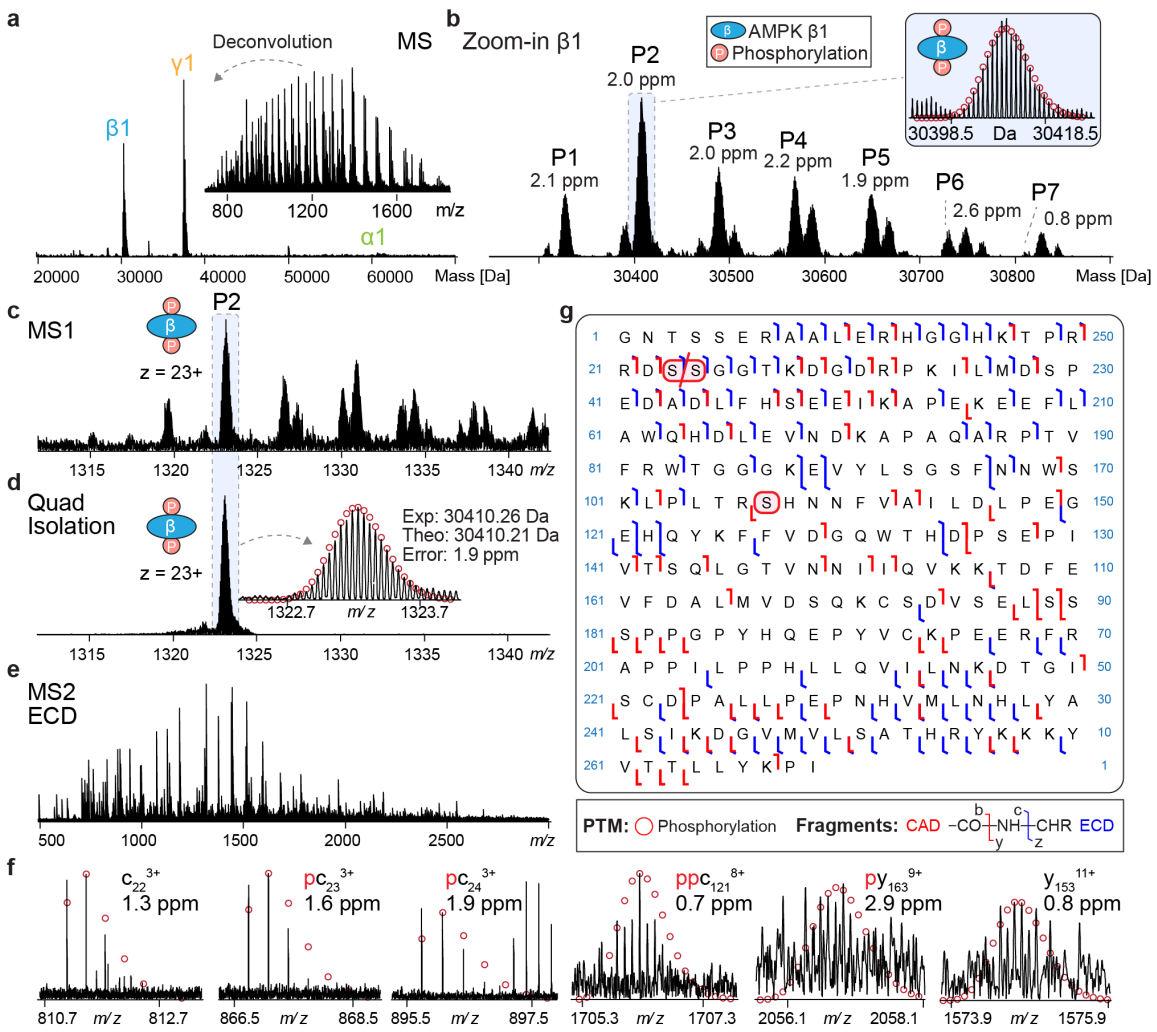

Figure 5: Top-down sequencing identifies doubly phosphorylated AMPK β1 proteoform architecture.

(a) Deconvoluted mass spectrum of denatured AMPK subunits with raw mass spectrum shown in inset. **(b)** Zoom-in shows isotopically resolved β1 phosphorylation states (1P-7P) with 2P as the most abundant species. **(c)** The 23+ charge state of the β1 shows a peak distribution similar to the deconvoluted spectrum in (b). **(d)** Quadrupole isolation of 2P β1 23+ precursor ion (1323 *m/z*) with isotopically resolved peak inset. **(e)** Representative ECD fragmentation spectrum showing extensive fragmentation pattern. **(f)** Selected fragment spectra (*p*: singly phosphorylated; *pp*: doubly phosphorylated). Mass errors are reported, and isotopic fittings are shown in red circles. Shift from fragment pattern c22, c23, c24 versus assigned positions pS24, pS25 due to N-terminal glycine cleavage. **(g)** Combined fragment map from

complementary CID and ECD experiments. Fragment notation: hook direction indicates type, color denotes method (blue: ECD, red: CID).

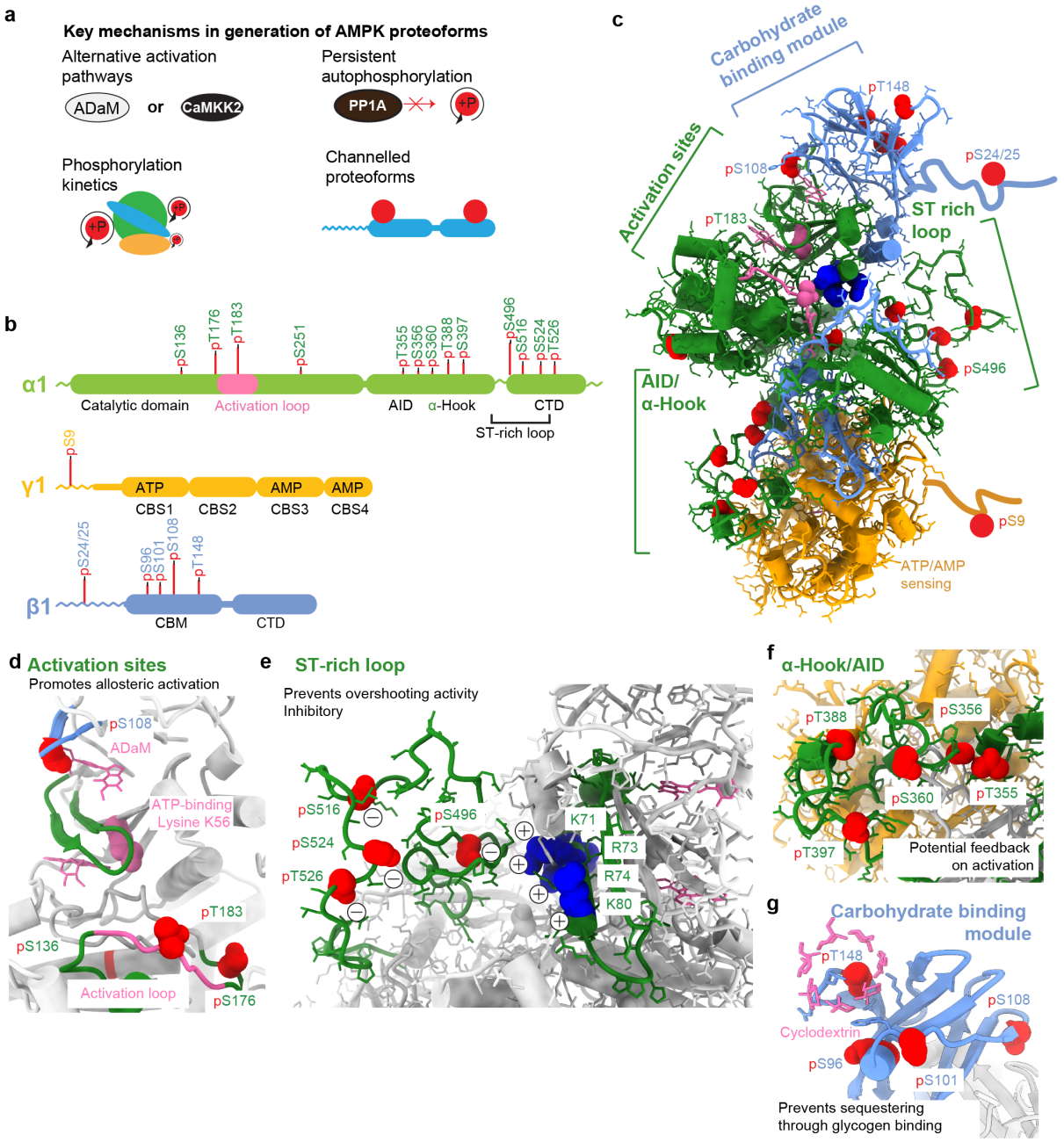

Figure 6. Integrated proteoform analysis reveals structural organization of AMPK phosphorylation networks and regulatory mechanisms.

(a) Key mechanisms contributing to AMPK proteoform generation illustrated. **(b)** Domain organization of AMPK α1β1γ1 subunit isoforms showing main functional domains and positions of identified phosphorylation sites. Red line heights represent relative

phosphorylation extent. Four CBS domains with nucleotide binding pockets here depicted in occupational state of activated enzyme. C-terminal domain (CTD). **(c)** AMPK α1β1γ1 protein structure homology model (Swiss-Model) based on PDB 5EZV and 4RER. Disordered termini represented as lines. Red spheres indicate identified phosphorylation sites clustered into four distinct structural hotspots. **(d)** Activation sites and catalytic center hotspot. Phosphorylations proximal to activation sites have critical regulatory functions. **(e)** ST-rich loop hotspot. Phosphorylation sites within this regulatory disordered region create electrostatic interactions with basic residues near the catalytic center, reducing T183 phosphorylation by upstream kinases and preventing activity overshooting through negative feedback. **(f)** Autoinhibitory domain (AID) and α-hook hotspot. This region facilitates allosteric communication between AMP binding at the γ-subunit and kinase domain activation. The identified phosphorylation cluster (T355, S356, S360, T388, S397) may constitute a feedback mechanism modulating AMP sensitivity and allosteric regulation. **(g)** Carbohydrate-binding module (CBM) hotspot. The CBM mediates AMPK sequestration at glycogen matrices. While β1-T148 has been functionally characterized for glycogen binding regulation, pS96 and pS101 remain uncharacterized but may influence CBM function due to structural proximity.

REFERENCES

1. Keenan, E. K., Zachman, D. K. & Hirschey, M. D. Discovering the landscape of protein modifications. *Mol. Cell* **81**, 1868–1878 (2021).
2. Walsh, C. T. *Posttranslational Modification of Proteins: Expanding Nature's Inventory*. (Roberts and Co. Publ, Englewood, 2006).
3. Smith, L. M. & Kelleher, N. L. Proteoform: a single term describing protein complexity. *Nat. Methods* **10**, 186–187 (2013).
4. Smith, L. M. *et al.* The Human Proteoform Project: Defining the human proteome. *Sci. Adv.* **7**, eabk0734 (2021).
5. Aebersold, R. *et al.* How many human proteoforms are there? *Nat. Chem. Biol.* **14**, 206–214 (2018).
6. Cohen, P. The origins of protein phosphorylation. *Nat. Cell Biol.* **4**, E127–E130 (2002).
7. Humphrey, S. J., James, D. E. & Mann, M. Protein Phosphorylation: A Major Switch Mechanism for Metabolic Regulation. *Trends Endocrinol. Metab.* **26**, 676–687 (2015).
8. Hu, L. *et al.* Pseudokinases can catalyse peptide cyclization through thioether crosslinking. *Nat. Chem.* 1–12 (2025) doi:10.1038/s41557-025-01954-1.
9. Steinberg, G. R. & Carling, D. AMP-activated protein kinase: the current landscape for drug development. *Nat. Rev. Drug Discov.* **18**, 527–551 (2019).
10. Nikolic, I., Leiva, M. & Sabio, G. The role of stress kinases in metabolic disease. *Nat. Rev. Endocrinol.* **16**, 697–716 (2020).
11. Melby, J. A. *et al.* Novel Strategies to Address the Challenges in Top-Down Proteomics. *J. Am. Soc. Mass Spectrom.* **32**, 1278–1294 (2021).
12. Bludau, I. *et al.* Systematic detection of functional proteoform groups from bottom-up proteomic datasets. *Nat. Commun.* **12**, 3810 (2021).
13. Phosphoproteomics in the Age of Rapid and Deep Proteome Profiling | Analytical Chemistry. https://pubs.acs.org/doi/10.1021/acs.analchem.5b04123.
14. Villén, J., Beausoleil, S. A., Gerber, S. A. & Gygi, S. P. Large-scale phosphorylation analysis of mouse liver. *Proc. Natl. Acad. Sci.* **104**, 1488–1493 (2007).
15. Humphrey, S. J., Azimifar, S. B. & Mann, M. High-throughput phosphoproteomics reveals in vivo insulin signaling dynamics. *Nat. Biotechnol.* **33**, 990–995 (2015).
16. Chen, B. *et al.* Coupling functionalized cobalt ferrite nanoparticle enrichment with online LC/MS/MS for top-down phosphoproteomics. *Chem. Sci.* **8**, 4306–4311 (2017).
17. Ge, Y., Rybakova, I. N., Xu, Q. & Moss, R. L. Top-down high-resolution mass spectrometry of cardiac myosin binding protein C revealed that truncation alters protein phosphorylation state. *Proc. Natl. Acad. Sci.* **106**, 12658–12663 (2009).
18. Lutomski, C. A. *et al.* Defining proteoform-specific interactions for drug targeting in a native cell signalling environment. *Nat. Chem.* **17**, 204–214 (2025).
19. Li, H., Nguyen, H. H., Ogorzalek Loo, R. R., Campuzano, I. D. G. & Loo, J. A. An integrated native mass spectrometry and top-down proteomics method that connects sequence to structure and function of macromolecular complexes. *Nat. Chem.* **10**, 139–148 (2018).
20. Tang, Q.-Q. *et al.* Sequential phosphorylation of CCAAT enhancer-binding protein β by MAPK and glycogen synthase kinase 3β is required for adipogenesis. *Proc. Natl. Acad. Sci.* **102**, 9766–9771 (2005).
21. Salazar, C. & Höfer, T. Multisite protein phosphorylation – from molecular mechanisms to kinetic models. *FEBS J.* **276**, 3177–3198 (2009).
22. Bilbrough, T., Piemontese, E. & Seitz, O. Dissecting the role of protein phosphorylation: a chemical biology toolbox. *Chem. Soc. Rev.* **51**, 5691–5730 (2022).

23. Steinberg, G. R. & Hardie, D. G. New insights into activation and function of the AMPK. *Nat. Rev. Mol. Cell Biol.* **24**, 255–272 (2023).
24. Trefts, E. & Shaw, R. J. AMPK: restoring metabolic homeostasis over space and time. *Mol. Cell* **81**, 3677–3690 (2021).
25. Ripa, R. *et al.* Refeeding-associated AMPKγ1 complex activity is a hallmark of health and longevity. *Nat. Aging* **3**, 1544–1560 (2023).
26. Steinberg, G. R. & Kemp, B. E. AMPK in Health and Disease. *Physiol. Rev.* **89**, 1025–1078 (2009).
27. Woods, A. *et al.* Ca2+/calmodulin-dependent protein kinase kinase-β acts upstream of AMP-activated protein kinase in mammalian cells. *Cell Metab.* **2**, 21–33 (2005).
28. Hawley, S. A., Russell, F. M. & Hardie, D. G. AMP-activated protein kinase can be allosterically activated by ADP but AMP remains the key activating ligand. *Biochem. J.* **481**, 587–599 (2024).
29. Yan, Y. *et al.* Structure of an AMPK complex in an inactive, ATP-bound state. *Science* **373**, 413–419 (2021).
30. Ovens, A. J. *et al.* Post-Translational Modifications of the Energy Guardian AMP-Activated Protein Kinase. *Int. J. Mol. Sci.* **22**, 1229 (2021).
31. Ross, F. A., MacKintosh, C. & Hardie, D. G. AMP-activated protein kinase: a cellular energy sensor that comes in 12 flavours. *FEBS J.* **283**, 2987–3001 (2016).
32. Neumann, D., Woods, A., Carling, D., Wallimann, T. & Schlattner, U. Mammalian AMP-activated protein kinase: functional, heterotrimeric complexes by co-expression of subunits in Escherichia coli. *Protein Expr. Purif.* **30**, 230–237 (2003).
33. Davies, S. P., Carling, D. & Hardie, D. G. Tissue distribution of the AMP-activated protein kinase, and lack of activation by cyclic-AMP-dependent protein kinase, studied using a specific and sensitive peptide assay. *Eur. J. Biochem.* **186**, 123–128 (1989).
34. Geoghegan, K. F. *et al.* Spontaneous alpha-N-6-phosphogluconoylation of a 'His tag' in Escherichia coli: the cause of extra mass of 258 or 178 Da in fusion proteins. *Anal. Biochem.* **267**, 169–184 (1999).
35. UniProt Consortium. UniProt: the universal protein knowledgebase in 2023. Nucleic Acids Res. 51, D523–D531 (2023).
36. Tuerk, R. D. *et al.* Tracking and quantification of 32P-labeled phosphopeptides in liquid chromatography matrix-assisted laser desorption/ionization mass spectrometry. *Anal. Biochem.* **390**, 141–148 (2009).
37. Warden, S. M. *et al.* Post-translational modifications of the β-1 subunit of AMP-activated protein kinase affect enzyme activity and cellular localization. (2001).
38. Mitchelhill, K. I. *et al.* Posttranslational Modifications of the 5′-AMP-activated Protein Kinase β1 Subunit*. *J. Biol. Chem.* **272**, 24475–24479 (1997).
39. Woods, A. *et al.* Identification of Phosphorylation Sites in AMP-activated Protein Kinase (AMPK) for Upstream AMPK Kinases and Study of Their Roles by Site-directed Mutagenesis *. *J. Biol. Chem.* **278**, 28434–28442 (2003).
40. Smiles, W. J. *et al.* AMPK phosphosite profiling by label-free mass spectrometry reveals a multitude of mTORC1-regulated substrates. *Npj Metab. Health Dis.* **3**, 8 (2025).
41. PhosphoSitePlus: Hornbeck, P.V. et al. PhosphoSitePlus, 2014: mutations, PTMs and recalibrations. Nucleic Acids Res. 43, D512–D520 (2015).
42. Garcia-Haro, L. *et al.* The PP1-R6 protein phosphatase holoenzyme is involved in the glucose-induced dephosphorylation and inactivation of AMP-activated protein kinase, a key regulator of insulin secretion, in MIN6 β cells. *FASEB J.* **24**, 5080–5091 (2010).

43. Gu, X. *et al.* Conformational heterogeneity of the allosteric drug and metabolite (ADaM) site in AMP-activated protein kinase (AMPK). *J. Biol. Chem.* **293**, 16994–17007 (2018).
44. Myers, R. W. *et al.* Systemic pan-AMPK activator MK-8722 improves glucose homeostasis but induces cardiac hypertrophy. *Science* **357**, 507–511 (2017).
45. Aledavood, E. *et al.* Understanding the Mechanism of Direct Activation of AMP-Kinase: Toward a Fine Allosteric Tuning of the Kinase Activity. *J. Chem. Inf. Model.* **59**, 2859–2870 (2019).
46. Hawley, S. A. *et al.* Phosphorylation by Akt within the ST loop of AMPK-α1 down-regulates its activation in tumour cells. *Biochem. J.* **459**, 275–287 (2014).
47. Desjardins, E. M. *et al.* The phosphorylation of AMPKβ1 is critical for increasing autophagy and maintaining mitochondrial homeostasis in response to fatty acids. *Proc. Natl. Acad. Sci. U. S. A.* **119**, e2119824119.
48. Oligschlaeger, Y. *et al.* The Recruitment of AMP-activated Protein Kinase to Glycogen Is Regulated by Autophosphorylation*. *J. Biol. Chem.* **290**, 11715–11728 (2015).
49. Larson, E. J. *et al.* MASH Native: a unified solution for native top-down proteomics data processing. *Bioinformatics* **39**, btad359 (2023).
50. Alexander, J. *et al.* Spatial Exclusivity Combined with Positive and Negative Selection of Phosphorylation Motifs Is the Basis for Context-Dependent Mitotic Signaling. *Sci. Signal.* **4**, ra42 (2011).
51. Miller, C. J. & Turk, B. E. Homing in: mechanisms of substrate targeting by protein kinases. *Trends Biochem. Sci.* **43**, 380–394 (2018).
52. Desjardins, E. M., Day, E. A., Scott, J. W. & Steinberg, G. R. Sensing of Long-Chain Fatty Acyl-CoA Esters by AMPK. in *Nutrient Sensing in Eukaryotes* (eds Russell, F. M. & Hardie, D. G.) 121–137 (Springer US, New York, NY, 2025). doi:10.1007/978-1-0716-4284-9_6.
53. Pearah, A. *et al.* Blocking AMPKαS496 phosphorylation improves mitochondrial dynamics and hyperglycemia in aging and obesity. *Cell Chem. Biol.* **30**, 1585-1600.e6 (2023).
54. Xiao, B. *et al.* Structural basis of AMPK regulation by small molecule activators. *Nat. Commun.* **4**, 3017 (2013).
55. Chan, H.-J. *et al.* Structural Heterogeneity of Proteoform-Ligand Complexes in Adenosine Monophosphate-Activated Protein Kinase Uncovered by Integrated Top-Down Mass Spectrometry. *J. Am. Chem. Soc.* (2025).
56. Yu, D., Peng, Y., Ayaz-Guner, S., Gregorich, Z. R. & Ge, Y. Comprehensive Characterization of AMP-Activated Protein Kinase Catalytic Domain by Top-Down Mass Spectrometry. *J. Am. Soc. Mass Spectrom.* **27**, 220–232 (2016).